© 2017. Published by The Company of Biologists Ltd | Journal of Cell Science (2017) 130, 2066-2077 doi:10.1242/jcs.198424

TOOLS AND TECHNIQUES

Chromatin organization at the nuclear periphery as revealed by image analysis of structured illumination microscopy data

Jindřiška Fišerová[1,*], Michaela Efenberková[2], Tomáš Sieger[3], Miloslava Maninová[1], Jana Uhlířová[1] and Pavel Hozák[1,4]

ABSTRACT

The nuclear periphery (NP) plays a substantial role in chromatin organization. Heterochromatin at the NP is interspersed with active chromatin surrounding nuclear pore complexes (NPCs); however, details of the peripheral chromatin organization are missing. To discern the distribution of epigenetic marks at the NP of HeLa nuclei, we used structured illumination microscopy combined with a new MATLAB software tool for automatic NP and NPC detection, measurements of fluorescent intensity and statistical analysis of measured data. Our results show that marks for both active and non-active chromatin associate differentially with NPCs. The incidence of heterochromatin marks, such as H3K27me2 and H3K9me2, was significantly lower around NPCs. In contrast, the presence of marks of active chromatin such as H3K4me2 was only decreased very slightly around the NPCs or not at all (H3K9Ac). Interestingly, the histone demethylases LSD1 (also known as KDM1A) and KDM2A were enriched within the NPCs, suggesting that there was a chromatin-modifying mechanism at the NPCs. Inhibition of transcription resulted in a larger drop in the distribution of H1, H3K9me2 and H3K23me2, which implies that transcription has a role in the organization of heterochromatin at the NP.

KEY WORDS: Structured illumination microscopy, Image analysis, Chromatin, Nucleus, Histone modification, Nuclear pore complexes

INTRODUCTION

The nuclear periphery (NP) represents a complex compartment of substantial importance for chromatin organization. Depending on its transcriptional status, chromatin has been shown to associate with different parts of the nucleus (Bickmore and van Steensel, 2013; Cavalli and Misteli, 2013). Among these, the nuclear envelope (NE) serves as a principal region for chromatin compartmentalization to which both active and inactive genes are targeted (Egecioglu and Brickner, 2011; Harr et al., 2016). In recent years, a substantial effort has been undertaken to understand the mechanism of chromatin targeting to the NE, including its causes and consequences. This paper is a contribution to the understanding of these interactions.

Chromatin organization inside a nucleus both reflects and influences the transcriptional activity of genes (Meldi and Brickner, 2011; Van Bortle and Corces, 2012). The way in which the chromatin is organized is influenced by a variety of factors and mechanisms including covalent modifications of N-terminal tails of histones, such as lysine acetylation (denoted Ac), lysine methylation (denoted me1, me2 and me3, for single, di- and tri-methylation respectively), serine phosphorylation and others (for a review, see Bannister and Kouzarides, 2011). Histone modifications act in diverse biological processes, such as transcriptional activation/inactivation, chromosome packaging, and DNA damage and repair pathways. Although the functions of many histone modifications have been elucidated, many still remain to be resolved. In general, the modifications H3K9me3, H2K9me, H3K27me2 and H3K27me3, as well as the recently described H3K23me2 (Vandamme et al., 2015), are associated with transcriptional silencing and formation of heterochromatin (Bannister and Kouzarides, 2011). The modifications associated with transcription activation are H3K4me3, H4K2me, H3K9Ac, H3K36me3 and H4K5Ac (Harr et al., 2016). The changes in histone modifications are directed by groups of enzymes responsible for addition or removal of the respective modification. Methyl groups are actively removed by histone demethylases, whereas removal of acetyl group is catalyzed by histone deacetylases (reviewed in Harr et al., 2016). There are two distinct families of mammalian histone demethylases with a growing number of their members often showing a functional overlap. Among them, LSD1 (also known as KDM1A) catalyzes demethylation of H3K4me1, H3K4me2, H3K9me1 and H3K9me2, and KDM2A demethylates H3K36me1 and H3K36me2 (Kooistra and Helin, 2012). These enzymes are thus part of the silencing machinery involved in chromatin organization inside the nucleus.

The nuclear lamina plays a significant role in the tethering of chromatin to the NE. Electron micrographs of eukaryotic nuclei show that, in most cells, condensed heterochromatin is enriched at the nuclear periphery (Reik, 2007; Ueda et al., 2014; Wu et al., 2005). Genome-wide mapping using DamID technology (Guelen et al., 2008; Pickersgill et al., 2006) or ChIP-seq (Sadaie et al., 2013; Shah et al., 2013, reviewed in Gruenbaum and Foisner, 2015) revealed that there are lamina-associated domains (LADs), genome regions of low gene density that are in contact with the lamina. In agreement with the characteristics of LADs as transcriptionally silent environments, repressive epigenetic histone modifications are commonly found at the nuclear periphery, including H3K9me2, H3K9me3, H3K27me2 and H3K27me3 (Eberhart et al., 2013; Kind et al., 2013; Wu et al., 2005; Yokochi et al., 2009).

Nuclear pore complexes (NPCs) are ∼100 MDa large multiprotein complexes that penetrate the NE to allow for regulated exchange of molecules between the nucleus and the cytoplasm (Raices and D'Angelo, 2012). They are composed of ∼30 different proteins called nucleoporins (Nups) that form the

[1]Department of Biology of the Cell Nucleus, Institute of Molecular Genetics CAS, v. v.i., Vídeňská 1083, Prague 142 00, Czech Republic. [2]Microscopy Centre – LM and EM, Institute of Molecular Genetics CAS, v.v.i., Vídeňská 1083, Prague 142 00, Czech Republic. [3]Department of Cybernetics, Faculty of Electrical Engineering, Czech Technical University in Prague, Prague, 121 35, Czech Republic. [4]Division BIOCEV, Institute of Molecular Genetics CAS, v.v.i., Průmyslová 595, Vestec, Prague 252 50, Czech Republic.

*Author for correspondence (fiserj@img.cas.cz)

Received 8 November 2016; Accepted 2 May 2017

Journal of Cell Science

Journal of Cell Science (2017) 130, 2066-2077 doi:10.1242/jcs.198424

central part of NPC passing thorough the NE, with cytoplasmic filaments emanating towards the cytoplasm and the nuclear basket directed towards the nucleoplasm. Recently, additional roles of NPCs and Nups in transcription regulation and chromatin organization have emerged (reviewed in Capelson and Hetzer, 2009; Pascual-Garcia and Capelson, 2014). In electron micrographs, zones adjacent to the NPCs appear as less dense in contrast to heterochromatin areas associated with the lamina (Belmont et al., 1993; Schermelleh et al., 2008). Consistent with this idea, Schermelleh et al. (2008) used 3D structured illumination microscopy to observe zones free of DAPI staining under the NPCs, suggesting a relationship between the NPCs and active genes. The existence of heterochromatin-free zones around the NPCs has been shown to be dependent on the presence of the nuclear pore protein TPR (Krull et al., 2010). According to the gene-gating hypothesis (Blobel, 1985), NPCs are able to specifically interact with, and possibly regulate, active sites of the genome to couple mRNA transcription and export. The evidence for a functional relationship between active genes and NPCs has been mostly shown in yeast. Inducible yeast genes, such as INO1, are targeted to the NPC upon activation, and this association was proven to be functionally important (Light et al., 2010; Taddei et al., 2006). In metazoa, genome-wide studies have reported a role for nucleoporins during development (reviewed in Talamas and Capelson, 2015). In human cells, Nup98 is targeted to genes that are active during stem cell differentiation (Kalverda et al., 2010; Liang et al., 2013). In contrast, the DamID profile of Nup98 in *Drosophila* found that Nup98 was predominantly at non-active genomic regions including insulator-binding sites (Kalverda et al., 2010). Several other studies have shown an association of NPCs with silenced genomic regions and chromatin boundary. Data from yeast and *Drosophila* revealed heterochromatin association with stable Nups, such as Nup100 or Nup84 (Galy et al., 2000; Ruben et al., 2011; Van de Vosse et al., 2013). In human HeLa cells, ChIP analysis of Nup93 also demonstrated that Nup93 interactions include silent gene regions marked by repressive histone modifications (Brown et al., 2008).

For the determination of detailed structural organization of the nucleus, structured illumination microscopy (SIM) has proven a respected super-resolution microscopy technique. The lateral resolution of SIM of ∼110–130 nm allows individual NPCs to be distinguished and, thus, SIM has been successfully adopted to investigate ultrastructural details of the NP, the nuclear lamina (Schermelleh et al., 2008; Shimi et al., 2008, 2015) and NPCs (Szymborska et al., 2013), as well as intranuclear architecture (Markaki et al., 2012).

In our approach, we used SIM in combination with image analysis followed by a robust statistical analysis of the data to discern the organization of chromatin at the NP in human HeLa cells. We were interested to determine whether there is any difference in the distribution of histones modified by groups defining active and inactive chromatin. Our data confirm the existence of heterochromatin exclusion zones around the NPCs and define the concrete modifications restricted within these zones. Moreover, our results prove that the pattern of individual histone marks around the NPCs has a non-random distribution, and show that histones modified with marks defining both active and non-active chromatin can associate with the NPCs. Interestingly, we also detected the presence of histone-modifying enzymes within the NPCs, implying that NPCs have a direct role in chromatin organization. Thus, our data highlight the importance of robust image analysis for the quality and preciseness of information based on super-resolution imaging and offer a detailed picture of chromatin organization at the NP in proximity to the NPCs.

RESULTS

Combination of structured illumination microscopy with image analysis enables the creation of a high-resolution map of the distribution of histone modifications in relation to NPCs

We used the SIM technique to acquire multichannel high-resolution images of the NP of human HeLa cells. We immunostained cells with a collection of antibodies against post-translationally modified histones to be detected with an excitation wavelength of 488 nm. For the detection of NPC positions, we used anti-Nup62 antibody in combination with Alexa-Fluor-555-coupled secondary antibody. DAPI, for heterochromatin visualization, was detected with an excitation wavelength of 405 nm (for details see Materials and Methods) (Fig. 1A). Combining these with SIM, enabled us to discern individual NPCs and their neighborhood. As we aimed at acquiring a statistically significant picture of the chromatin organization around the NPCs, we programmed a script in MATLAB software for an automatic NPCs segmentation and determination of the NE position in central sections of the *z*-stacks (Fig. 1B–D; Fig. S1). The segmentation was followed by determination of NP regions of two kinds: (1) areas associated with NPCs [hereafter referred to as measured area for NPCs, denoted mNPCs; Fig. 1D] and (2) NPC-free areas associated with the nuclear envelope [hereafter referred to as measured area for the NE, denoted mNE; Fig. 1D; for details, see Materials and Methods]. The fluorescence intensity of the respective histone modification [or other proteins of interest such as lamin B1 or HP1a (also known as CBX5)] was collected and normalized (see Materials and Methods), and the median fluorescence intensity values of mNPCs and mNE were presented as heat maps (Fig. 1E,F for DAPI). To compare the histone organization at mNPCs to that at mNE, the median fluorescence intensities of mNE were subtracted from the median fluorescence intensities of mNPCs. The resulting difference between mNPCs and mNE was plotted as a heat map (Fig. 1G) and the regions showing a statistically significant difference in fluorescence intensity between mNPCs and mNE were highlighted (Fig. 1G, yellow line; for details, see Materials and Methods). We carried out several testing experiments to confirm the method validity. Fig. 2A–D shows that the fluorescence intensity of DAPI is significantly reduced in the area surrounding NPCs, which is in accordance with previous observations (Krull et al., 2010; Schermelleh et al., 2008) and thus supports the legitimacy of our approach. The size of the area with the reduced fluorescence intensities of DAPI at the NPC neighborhood is ∼360 nm towards the nuclear interior and 200 nm along the NP. Hereafter, we call the zones around NPCs with reduced amount of heterochromatin ‘exclusion zones’. In addition, to describe the dimensions of the area surrounding the NPCs, we always refer to the total size of the area including the position of the NPC basket as described above.

To further confirm the relevance of the method, we analyzed the localization of TPR, a protein of the NPC basket, in respect to the Nup62 to confirm that the method can positively detect the localization of TPR in relation to the position of Nup62. Fig. 2E–H shows an enrichment of the TPR at the NPC baskets and in close proximity to them, thus validating the method used. We also analyzed the position of lamin B in respect to the position of Nup62. The lamin B was excluded from the area of the NPC baskets and their nearest neighborhood, as expected (Fig. 2I–L). Taken together,

Journal of Cell Science (2017) 130, 2066-2077 doi:10.1242/jcs.198424

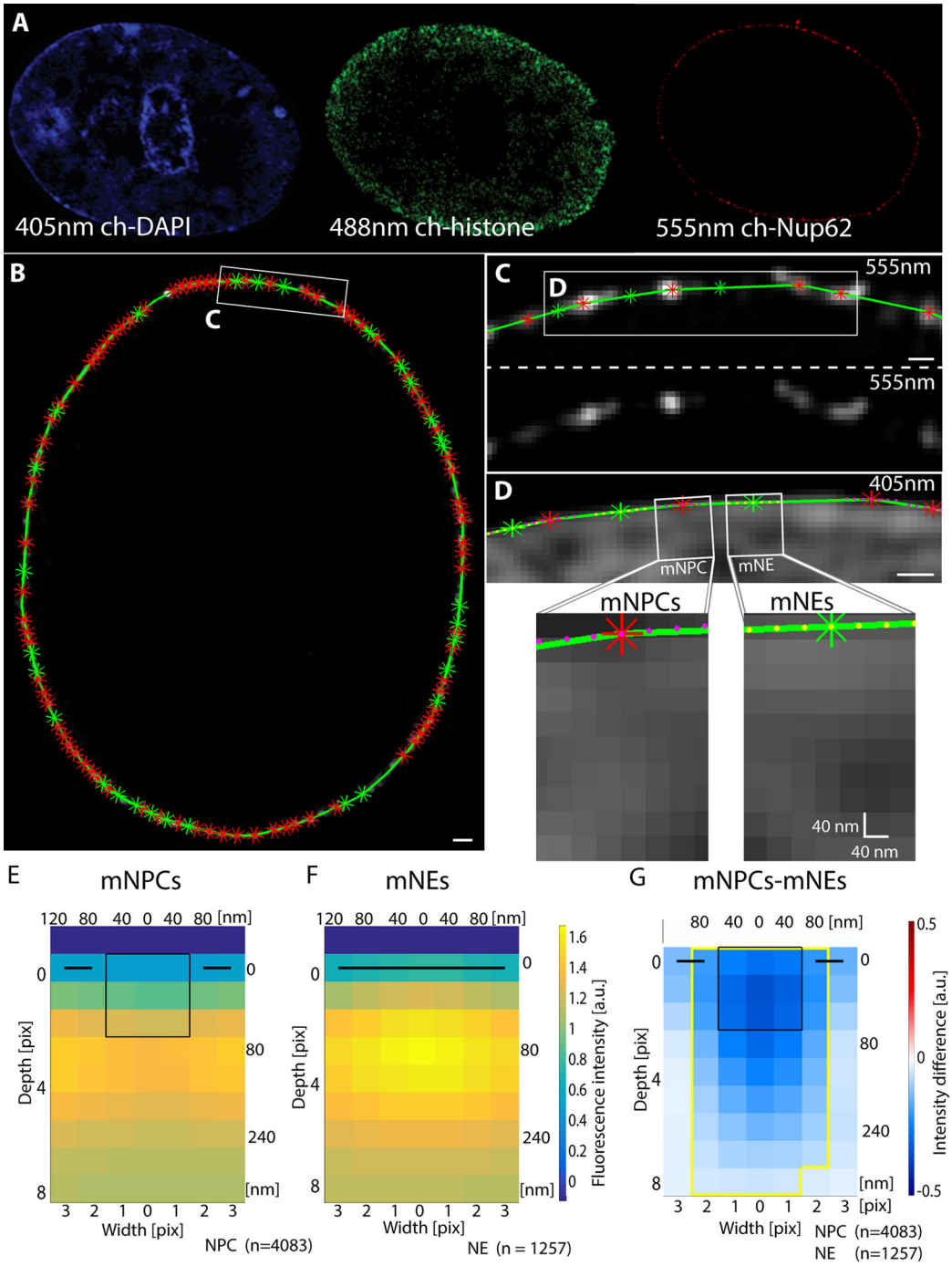

Fig. 1. The principle of the image analysis. (A) HeLa cells were stained with DAPI to detect DNA with an excitation wavelength of 405 nm (405nm ch), and were immunostained for post-translationally modified histones, to be detected with an excitation wavelength of 488 nm (488nm ch), and Nup62, for NPC detection using a wavelength of 555 nm (555nm ch). (B,C) NPCs were segmented (red stars) and the position of the NE (green line) and regional intensity minima at the NE (green stars) were determined by using MATLAB (for details, see Materials and Methods). The bottom panel shows the data for the respective area only. (D) Areas for fluorescence intensity data collection were determined in the 405 nm channel (DAPI, shown) or 488 nm channel (histone modification detection). Yellow dots correspond to the position of the first row of pixels of the mNEs (measured area at the NE), whereas magenta dots correspond to individual pixels of the first row of mNPCs (measured area at the NPC). White rectangles mark the positions of the mNPC and mNE. Dimensions of 1 pixel are indicated. (E,F) The plots display the median fluorescence intensity values of DAPI at the mNPCs (E) and mNEs (F) colored using a heat map. The positions of the NPC and NE are indicated within each plot (black square and black line, respectively) as well as '*n*', the number of pooled mNPCs and mNEs. The *x* and *y* axes represent individual pixels along the nuclear envelope (*x*) and towards the nuclear interior (*y*). (G) The median fluorescent intensity values of mNEs (shown in F for DAPI) were subtracted from the median fluorescence intensity values of mNPCs (shown in E for DAPI). The result was plotted using a heat map to show areas with positive values (meaning higher fluorescence intensity at mNPCs) in red and negative values (higher fluorescence intensity at mNEs) in blue. In case of DAPI, the fluorescence intensity at NPCs is lower than at the NE, thus, the resulting color of the squares within the plot is blue. The significantly different area (after FDR adjustment for multiple comparison) is bordered in yellow. The position of the NPC and NE is indicated within each plot (black square and black line, respectively) as well as '*n*', the number of pooled NPCs and NEs. The *x* and *y* axes represent individual pixels along the nuclear envelope (*x*) and towards the nuclear interior (*y*). Scale bars: 1 µm (B), 200 nm (C,D).

Journal of Cell Science (2017) 130, 2066-2077 doi:10.1242/jcs.198424

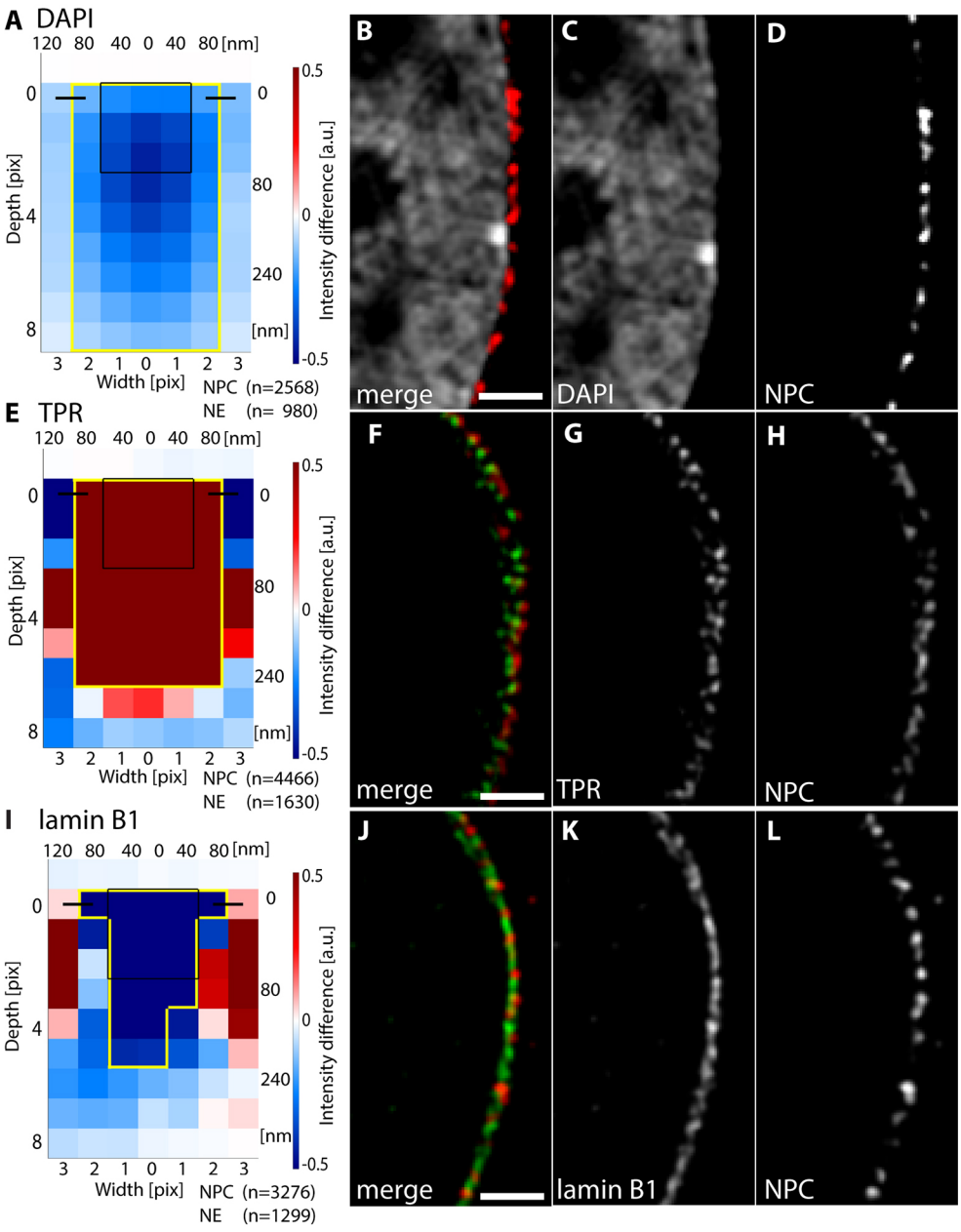

Fig. 2. The distribution of DAPI, TPR and lamin B1 around NPCs. (A,E,I) The heat-maps show the difference in the median fluorescence intensity values for DAPI (A), TPR (E) and lamin B1 (I) between the mNPCs and mNEs. Positive values (where the fluorescent intensity at mNPCs is greater than the intensity at mNEs) are shown as shades of red, negative values as shades of blue. Significantly different areas (after FDR adjustment for multiple comparison) are bordered in yellow. For better orientation, the position of the NPC and NE is indicated (black square and black line, respectively). (B–D,F–H,J–L) The examples of the respective OMX-SIM images. Merged (B,F,J) and individual channels for DAPI (C), TPR (G), lamin B1 (K) and Nup62 (D,H,L) are shown. Scale bars: 1 µm.

our method enables us to precisely detect the incidence of the protein of interest at the NPCs with respect to the NP.

Histones modified with marks for active and inactive chromatin locate differently in the proximity of NPCs

Using the above-described approach, we asked about the organization of chromatin around NPCs in terms of the distribution of modified histones. First, we tested the distribution of the linker histone H1 and modified histones H3K27me2, H3K9me2 and H3K23me2, all of which are considered as markers of transcriptionally inactive chromatin. As expected, most of the tested histones were excluded from the NPCs and from the area associated with the NPC baskets (Fig. 3). In more detail, the ‘exclusion zone’ for H3K27me2, H3K9me2 and H1 was up to 320 nm long and 200 nm wide (Fig. 3A–F). Surprisingly, H3K23me2 was significantly enriched within the NPC baskets (Fig. 3G,H) similarly to HP1a (Fig. 3I,J). Thus, the size of NPC exclusion zones differs even for individual modified histones associated with silent chromatin.

Next, we were interested in determining whether the modifications denoting active chromatin can interfere with the NPCs baskets, and we thus tested several modifications previously shown to be associated with active transcription, including H3K4me2, H4K5Ac, H3K36me3 and H3K9Ac. Interestingly, for the histone modifications of H3K4me2, H4K5Ac and H3K36me3, we also detected an exclusion zone (Fig. 4A–H). For the histone modifications of H3K4me2 and H4K5Ac, the exclusion was limited to the NPC baskets and closely associated areas up to 40 nm distant from the NPC baskets, indicating that although the euchromatin incidence within the NPC baskets is restricted, it can be present in close proximity to the NPC (Fig. 4A–D). The exclusion zone for H3K36me3 was a little larger, reaching 200 nm towards the nuclear interior (Fig. 4E). Finally, the H3K9Ac modification showed no difference in fluorescence intensity between the mNPC and mNE

Journal of Cell Science (2017) 130, 2066-2077 doi:10.1242/jcs.198424

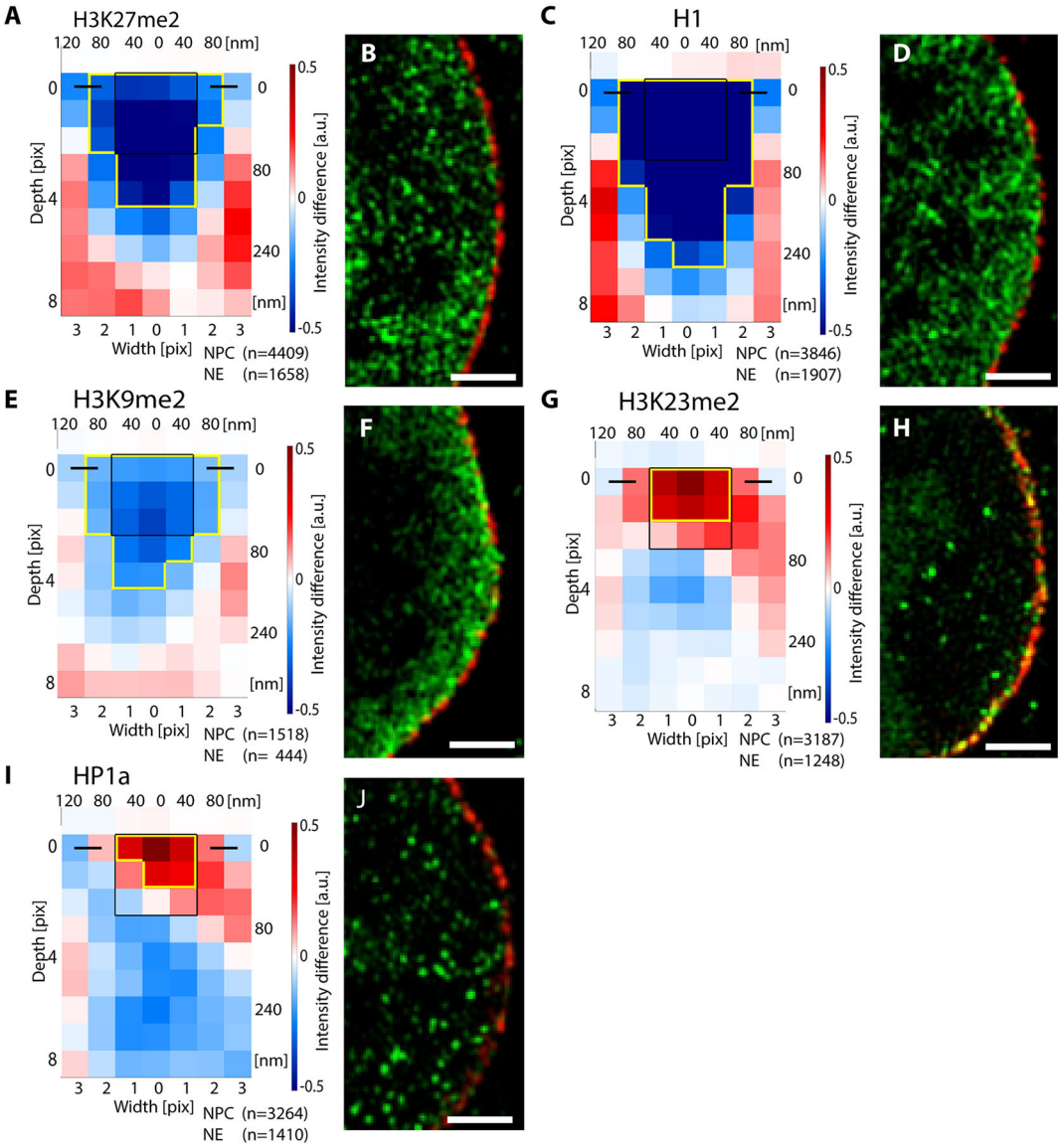

Fig. 3. The distribution of histones modified with inactive marks around NPCs in HeLa cells. (A,C,E,G,I) The heat-maps show the difference in median fluorescence intensity values for H3K27me2 (A), H1 (C), H3K9me2 (E), H3K23me2 (G) and HP1a (I) between the mNPCs and mNEs. Positive values are shown as shades of red, negative values as shades of blue. Significantly different areas (after FDR adjustment for multiple comparison) are bordered in yellow. For better orientation, the position of the NE and NPCs is indicated (black square and black line, respectively). '*n*' is indicated within each plot. (B,D,F,H,J) Examples of the respective OMX-SIM images. The modified histones are colored in green, Nup62 is depicted in red. Scale bars: 1 µm.

(Fig. 4G,H), which suggests that H3K9Ac does not discriminate between a transcriptionally repressive and permissive environment at the NP.

Thus, our results show that chromatin modified by marks associated with silent heterochromatin was mostly strictly excluded from the NPCs and the surrounding areas, except for H3K23me2. In contrast, the distribution of euchromatin marks around the NPCs was rather variable with larger permissive zones (H3K36me3), permissive zones just touching at the NPCs (H4K5Ac and H3K4me2), or not discriminating for NPCs and NP (H3K9Ac).

Histone demethylases LSD1 and KDM2A are enriched at the NPCs

Our data showed that the NPCs are generally void of mono- and di-methylated H3. Thus, we were interested in whether the respective enzymes responsible for removing mono- and di-methyl groups are located within the NPC and the NPC-associated areas and, therefore, whether the chromatin can be post-translationally modified within the NPC. Therefore, we performed the MATLAB image analysis on HeLa cells immunostained for the histone demethylases LSD1 (which recognizes H3K4me1, H3K4me2, H3K9me1 and H3K9me2) and KDM2A (recognizing H3K36me1 and H3K36me2). The results showed that both KMD2A were enriched within NPC baskets in comparison to mNE (Fig. 5). Thus, our results support the hypothesis of the presence of the chromatin-modifying enzymes within the NPC.

The organization of H1, H3K9me2 and H3K23me2 at the NPCs is dependent on transcription

The NPCs are generally viewed as the transcriptionally active compartments at the NP. In the gene-gating hypothesis (Blobel, 1985), the NPCs were predicted to serve as scaffolds for active

Journal of Cell Science (2017) 130, 2066-2077 doi:10.1242/jcs.198424

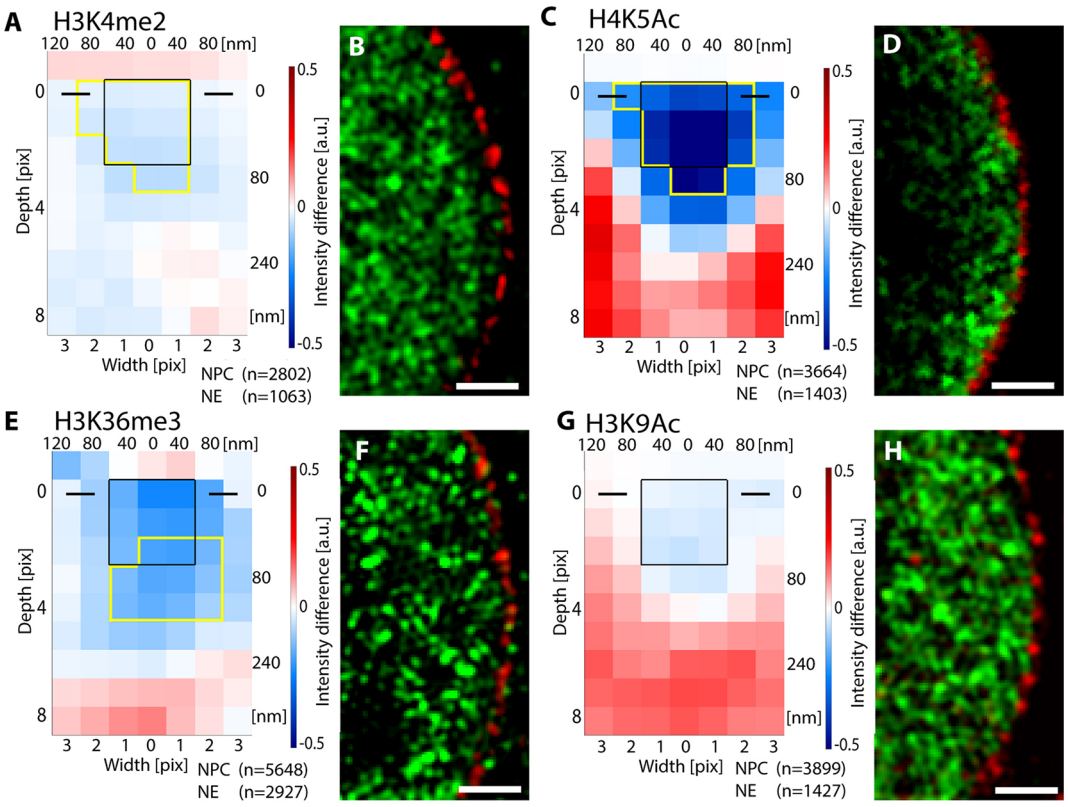

Fig. 4. The distribution of histones modified with active marks around NPCs in HeLa cells. (A,C,E,G) The heat-maps show the difference in median fluorescence intensity values for H3K4me2 (A), H4K5Ac (C), H3K36me3 (E) and H3K9Ac (G) between the mNPCs and mNEs. Positive values are shown as shades of red, negative values as shades of blue. Significantly different areas (after FDR adjustment for multiple comparison) are bordered in yellow. For better orientation, the position of the NE and NPC is indicated (black square and black line, respectively). '*n*' is indicated within each plot. (B,D,F,H) Examples of the respective OMX-SIM images. The modified histones are colored in green, Nup62 is depicted in red. Scale bars: 1 µm.

genes to be transcribed in a close proximity to their transportation to the cytoplasm. We hypothesized that transcription might affect the chromatin organization at the NP. To test the role of active transcription by RNA polymerase II on chromatin organization at the NP, we treated cells with the RNA polymerase II inhibitor actinomycin D (AMD; see Materials and Methods). The most-apparent impact of AMD was observed for the distribution of the inactive histone modifications, including the distribution of H1 and H3K9me2, as well as DAPI (Fig. 6A–F; Fig. S2A–C). In those cases, we observed a significant drop in the incidence of the respective proteins around the NPCs and enlargement of voids around NPCs. Moreover, the incidence of inactive modification H3K23me2, which was enriched at the NPCs in the control condition, decreased significantly (Fig. 6G–I). This result indicates that the arrangement of silent chromatin linked with H1, H3K9me2 as well as H3K23me2 at NPCs relates to transcription. Finally, no difference in mNPC or mNE distribution was observed for H3K27me2 (Fig. S2D–F). Surprisingly, we observed no or very mild difference in mNPC and mNE distribution after AMD treatment for any of the active modifications tested (H4K5Ac, H3K4me2, H3K9Ac and H3K36me3; Fig. S2G–L and not shown) suggesting that the presence of these modifications at the NP and around the NPCs is not dependent on transcription.

DISCUSSION

We present a combination of SIM with image analysis and statistical evaluation, and show this approach can provide highly valuable insights into the chromatin organization at the NP. The ability of SIM to resolve individual nuclear pores, and detect and measure some chromatin and nuclear lamina features has been shown previously (Schermelleh et al., 2008). Here, by employment of image analysis and statistical evaluation of the data, we demonstrate a further increase in the extraction of the biological data, and thus detection of new details in nuclear structures. Thus, our approach demonstrates new possibilities for SIM and illustrates a potential for data mining fluorescence images.

Immunofluorescence as a method of structural detection has advantages and disadvantages. It allows for stable and strong fluorescence necessary to get SIM images of the appropriate quality with a high signal-to-noise ratio. In this approach, the top quality of the images is a must and, therefore, a careful control of all the steps necessary to gain the best quality images is a necessary prerequisite (Waters, 2009). Importantly, our method can reliably detect voids in DAPI staining as well as a drop in lamin B around NPCs. The very same result has previously been described (Schermelleh et al., 2008), who used, in principle, a similar approach of SIM imaging and straightforward image analysis. Our approach also clearly detects the relative localization of Nup62 and TPR, distinct components of the NPCs. Whereas the Nup62 is part of the NPC core and accordingly is located within the NPC center (Strambio-De-Castillia et al., 2010), TPR is positioned more distally away from the NPC center being one of the constituents of NPC basket (Frosst et al., 2002; Krull et al., 2010). In accordance with this, we detected TPR as being located within the NPC basket and 120–160 nm distally towards the nuclear interior, which additionally argues in favor of the approach.

Journal of Cell Science (2017) 130, 2066-2077 doi:10.1242/jcs.198424

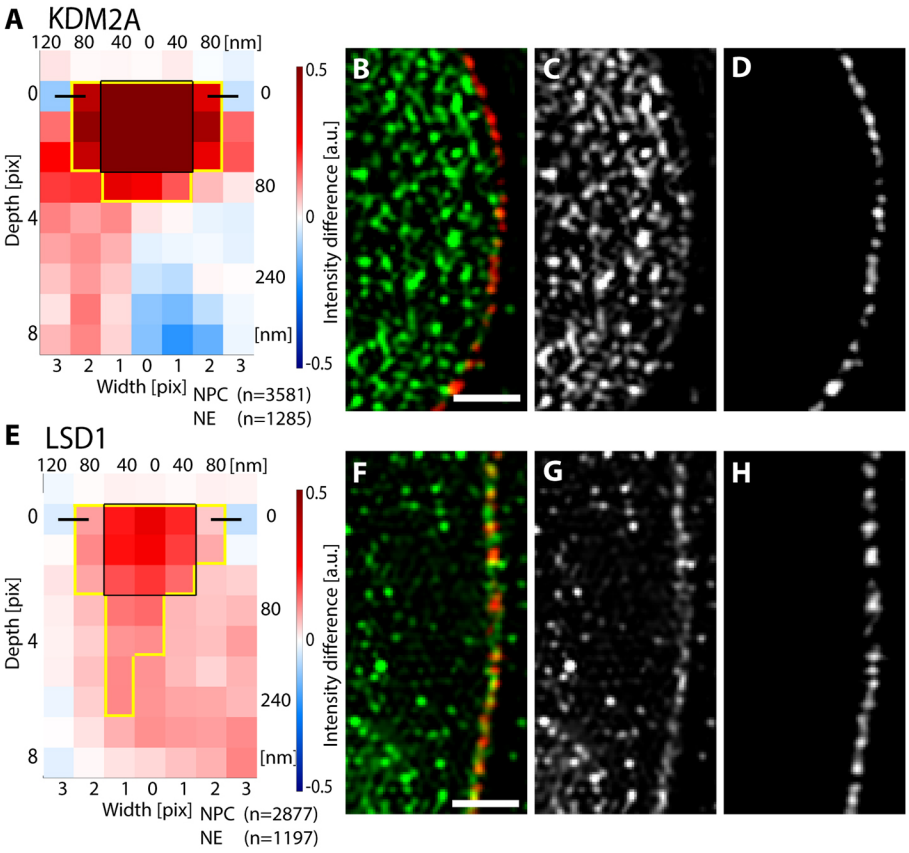

Fig. 5. The distribution of histone demethylases KDM2A and LSD1 around the NPCs. (A,E) The heat-maps show the difference in median fluorescence intensity values for KDM2A (A) and LSD1 (E) between the mNPCs and mNEs. Positive values are shown as shades of red, negative values as shades of blue. Significantly different areas (after FDR adjustment for multiple comparison) are bordered in yellow. For better orientation, the position of the NE and NPC is indicated (black square and black line, respectively). '*n*' is indicated within each plot. (B–D,F–H) Examples of the respective OMX-SIM images. Merged (B,F) and individual channels for KDM2A (C) LSD1 (G) and Nup62 (D,H) are shown. Scale bars: 1 µm.

A parallel method for assessing localization of histone modifications detection, such as immunogold labeling for transmission electron microscopy (TEM), would strengthen our data. We have attempted to use immunogold labeling of both high-pressure frozen and freeze-substituted HeLa cells, as well as chemically fixed HeLa cells; however, apart from the detection of histone H1 (Fig. S3A), we could not acquire any signal on TEM sections (data not shown). Electron micrographs of HeLa nuclei stained with anti-H1 antibody confirmed our immunofluorescence data, showing strong H1 staining at the NP with voids of signal at the NPCs and in their proximity (Fig. S3A, dotted line). The size of the voids (~150–180 nm in width and 150–280 nm in length) agreed with our light microscopy data, which showed an average distance of ~200 nm in width and up to 320 nm in length. Thus, TEM experiments confirmed the existence of an exclusion zone for histone H1 around NPCs.

Another aspect of the approach, the resolution of images captured by SIM (up to 110–120 nm), means that, in fact, the data still only provide a coarse approximation to the reality within a cell. The disadvantage of the relatively lower resolution in comparison to other super-resolution techniques, such as stimulation emission depletion (STED), is balanced by the speed of the acquisition of SIM multicolor images, which, in turn, enables the acquisition of high numbers of mNPCs and mNE (several thousands) for a statistical analysis, which would require considerably more time investment using, for example, STED.

The statistical analysis itself ensures that the data provide highly relevant structural information. Although the biological information at the individual NPC level is dimed by averaging of all NPCs, the averaging is justified. This is because there is no direct evidence for the existence of individual categories of NPCs, though individual NPCs might differ in their state of transport (number of transported molecules etc.). Although Iborra et al. (2000) have suggested that two populations of NPCs, specific for import and export, exist, no further proof of distinct types of NPCs within one nucleus has been provided since. Thus, the averaging, an inherent component of many biological methods, including genome-wide screens, was performed, which meant that we could more accurately determine the characteristics shared by all NPCs and perform a more-sensitive comparison of mNPCs and mNE areas. It is worth mentioning that NPCs are closely spaced on the nuclear envelope and, therefore, we were able to detect a lower amount of mNE in comparison to the mNPCs.

By means of super-resolution imaging, we provide a detailed picture of the intranuclear distribution of histones modified with a set of post-translational modifications. Despite the resolution power of super-resolution imaging, it remains challenging to discern the function of the detected immunolabeled spots of modified histones. In agreement with previous studies, we observed heterochromatin arranged along the NE in HeLa cells (Fig. S3B) and confirmed the decreased incidence of heterochromatin in close proximity to the NPC in comparison to the NPC-free areas at the NE (Belmont et al., 1993). The heterochromatin of HeLa cells was arranged in a quite thin layer with rather open heterochromatin exclusion zones around the NPCs. Varying shades of gray within the nuclear interior in electron micrographs suggest varying condensation states for chromatin in the nucleus. Our fluorescence microscopy study further supported and extended the electron microscope observations. We showed that the decreased concentration of heterochromatin is associated with prominently H1 and H3K27me2 and to a lesser extent H3K9me2, as well as some active euchromatin marks including H3K4me2, H4K5Ac or H3K36me3. The schematic distribution of modified histones

Journal of Cell Science (2017) 130, 2066-2077 doi:10.1242/jcs.198424

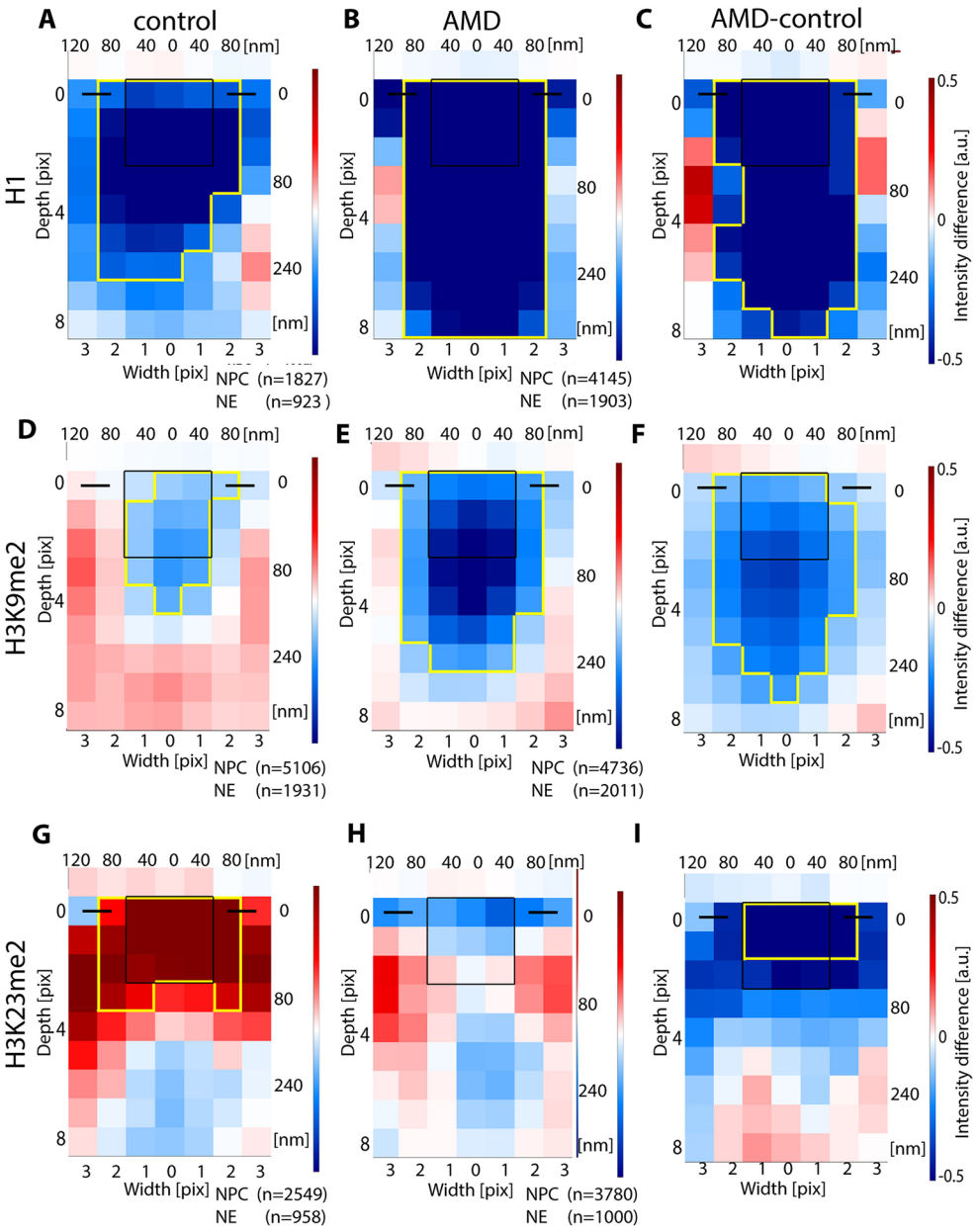

Fig. 6. The effect of AMD treatment on chromatin organization around NPCs in HeLa cells. The heat-maps show the differences in median fluorescence intensity values for H1 (A–C), H3K9me2 (D–F) and H3K23me2 (G–I) between the mNPCs and mNEs in control and in AMD-treated cells. Positive values are shown as shades of red, negative values as shades of blue. For better orientation, the position of the NE and NPC is indicated (black square and black line, respectively). Control data are shown in A, D and G; AMD-treated cells are shown in B, E and H. (C,F,I) The heat-maps display the difference in fluorescence intensity median values of mNPCs and mNEs in control and AMD-treated cells, e.g. fluorescence intensity values of control data were subtracted from fluorescence intensity values of AMD data. The significantly different areas on FDR-adjusted *P*-values are bordered in yellow. '*n*' is indicated within each plot.

around NPCs is demarcated in Fig. 7. The width, as well as the height, of the NPC exclusion zone we measured (i.e. 200 nm and 240–280 nm) was approximately twice as long as the dimensions found for the heterochromatin exclusion zone by Krull et al. (2010) (~119 nm and 107 nm). The more-condensed heterochromatin around NPC found by Krull et al. (2010) is likely the result of the infection of HeLa cells by poliovirus in order to force heterochromatin formation (Krull et al., 2010). Interestingly, the exclusion zone we detected overlapped with the localization of the TPR. This further supports the hypothesis of Krull et al. (2010) that TPR plays a role in forming the heterochromatin scaffold.

Our investigations further showed that the NPC exclusion zone for active modifications was smaller in comparison to that for inactive histone modifications. Thus, euchromatin labeled with H3K4me2 or H4K5Ac can reach to the NPC or even enter the NPC baskets more freely. The presence of histones modified by active marks in very close proximity to the NPC further suggests the existence of a transcriptionally active or potentially active zone located very near to the NPC. Additionally, the H3K9Ac mark does not discriminate at all between the NPCs and the NPC-free areas at the NE, indicating genes marked by H3K9Ac might get easier access to the NPCs. Our results imply that the distribution of both the heterochromatin and the active chromatin are regulated at the proximity of the NPC. Even though the presence of chromatin-free channels connected to the NPCs has been suggested previously (Visser et al., 2000) our data instead favor the hypothesis of a regulated incidence of both condensed and de-condensed chromatin.

We found that H3K23me2, as well as HP1a, was enriched within the NPC, which might indicate that H3K23me2 is important for transport-associated processes. The presence of H3K23me2 in *C. elegans* has been shown to correlate with regions that have H3K9me3 and heterochromatic regions (Vandamme et al., 2015). However, information on mammalian cells is scarce. The transcription block significantly affected the distribution specifically of H3K23me2 in addition to H1 and H3K9me2, which implies that the modifications are involved in transcription-

Journal of Cell Science (2017) 130, 2066-2077 doi:10.1242/jcs.198424

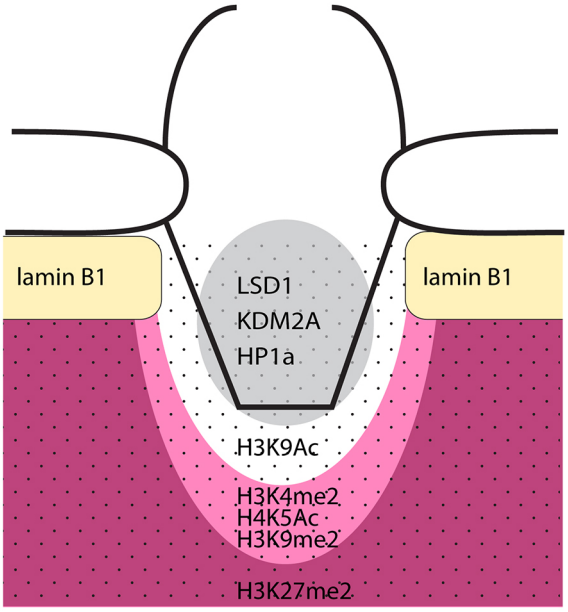

Fig. 7. A schema of the distribution of chromatin around the NPCs. The incidence of histone modifications at the NPCs in relation to the NE, as tested in this work is schematically depicted. Heterochromatin modifications of H3K27me2 and histone H1 (dark magenta) form larger exclusion zones around NPCs in comparison to H3K9me2 and the euchromatin marks (H3K4me2, H3K36me3 and H4K5Ac; light magenta) whereas H3K9Ac (dotted area) shows no difference in the distribution at NPC versus NE. The higher incidence of histone demethylases, HP1a and H3K23me2 (gray) within the NPCs is also indicated, as well as the presence of lamin B1 (pale yellow) at the NE.

related processes at the NPCs. Mechanisms of heterochromatin formation have been shown to be transcriptional dependent. In yeast, the heterochromatic repeats need to be transcribed to generate siRNA that positively regulates heterochromatin formation (Volpe et al., 2002). A similar system has been described in *Drosophila* (Pal-Bhadra et al., 2004; van Rij et al., 2006; Wang et al., 2006). The described mechanisms involve deactylation of H3K9Ac by HDAC1, demethylation of H3K4 by LSD1 and KDM2A, methylation of H3K9 or H3K23 and binding of HP1 (Schotta et al., 2004). Accordingly, we have found that members of this machinery, including HDAC1 (data not shown), LSD1 and KDM2A, were present within the NPCs more abundantly than at the NE. In addition, in metazoan cells, Nup155 was identified as a histone deacetylase 4 (HDAC4)-interacting protein, and the interaction proved to be important for gene expression (Kehat et al., 2011). The presence of more components of the silencing machinery within the NPC favors the hypothesis whereby NPCs serve as a scaffold for histone-modifying enzymes and thus are involved in the formation of both heterochromatin and euchromatin. However, such a hypothesis needs further verification.

In this work, we mapped the distribution of chromatin at the NP in relation to the NPCs. By combination of SIM and extensive image analysis, we explored the possibilities of SIM and observed an organizational pattern of individual histone modifications around NPCs. Importantly, the approach enabled us to detect the presence of H3K23me2 and chromatin-modifying enzymes to be specifically present at NPCs. However, more investigation would be necessary to resolve the exact role of the individual modifications at the NPCs as well as provide more mechanistic details on the formation of heterochromatin and euchromatin, and their distribution at the NP.

MATERIALS AND METHODS

Cell line, inhibitors and antibodies

Adherent human cervical carcinoma (HeLa) cells (obtained from the American Type Culture Collection, ATCC) were grown on glass coverslips (Marienfeld, Lauda-Königshofen, Germany) (rectangular, 18 mm in diameter, 170±5 µm thickness) in Dulbecco's modified Eagle's medium (DMEM; Sigma-Aldrich, St Louis, MO) supplemented with 10% fetal bovine serum (Sigma-Aldrich) at 37°C in 5% CO_2 humidified atmosphere. To inhibit RNA polymerase II, actinomycin D (Sigma-Aldrich) was added to the medium at a concentration of 1 µg/ml for 4 h.

Antibodies

Primary antibodies were as follows: anti-H4K5Ac rabbit polyclonal IgG (07-327, Millipore-Merk, Darmstadt, Germany, 1:300); anti-H3K9Ac rabbit polyclonal IgG antibody (ab10812, Abcam, Cambridge, UK, 1:300); anti-H4K20me1 rabbit polyclonal IgG antibody (ab9051, Abcam, 1:300); anti-H3K4me2 rabbit polyclonal IgG antibody (07-030, Millipore-Merk, 1:300); anti-H3K9me2 rabbit polyclonal IgG antibody (17-648, Millipore-Merk, 1:300); anti-H3K27me2 rabbit polyclonal IgG (ab24684, Abcam, 1:300); anti-H3K23me2 rabbit polyclonal IgG (39653, Active motif, Carlsbad, USA, 1:300); anti-H3K36me2 rabbit polyclonal IgG (ab9049, Abcam, 1:300); anti-H1 mouse polyclonal IgG (ab71594, Abcam, 1:100); anti-lamin B1 rabbit polyclonal IgG (ab16048, Abcam, 1:100); anti-HP1a mouse monoclonal IgG (05-689, Millipore-Merk, 1:100); anti-HP1a goat polyclonal IgG (ab77256, Abcam, 1:100); anti-LSD1 rabbit polyclonal IgG (C69G12, Cell Signaling Technology, Danvers, MA, 1:200); anti-KDM2A rabbit polyclonal IgG (NBP1-78305, Nuovus Biologicals, Littleton, CO, 1:200); anti-TPR rabbit polyclonal IgG (ab84516, Abcam, 1:200); anti-Nup62 rat monoclonal IgG (ab188413, Abcam, 1:500).

To ensure the signal specificity of the primary antibodies, we have carefully selected the antibodies that have been validated previously on dot blots and western blots (anti-H4K5Ac, anti-H4K20me1, anti-H3K4me2, anti-H3K9me2, anti-H3K27me2 and anti-H3K36me3; data available at Antibody Validation Database, http://compbio.med.harvard.edu/antibodies/) (Egelhofer et al., 2011) or that have been successfully used for immunofluorescence by others. We have also performed western blots to further test the antibody specificity (Fig. S4).

Secondary antibodies were as follows: goat anti-rabbit IgG (H+L) antibody conjugated to Alexa Fluor 488 (A11034, Invitrogen, Carlsbad, USA), goat anti-rat IgG (H+L) antibody conjugated to Alexa Fluor 488 (A21434, Invitrogen), goat anti-mouse IgG (H+L) antibody conjugated with Alexa Fluor 488 (A21236, Invitrogen).

Indirect immunofluorescence for super-resolution fluorescence microscopy

HeLa cells seeded on square glass coverslips as above were grown to 70–80% confluence and washed with phosphate buffered saline (PBS) twice for 4 min each time at room temperature (RT), fixed in 3% paraformaldehyde in PBS and washed again with PBS twice for 4 min at RT. Following permeabilization with 0.1% Triton X-100 in PBS for 20 min and washes in PBS (three times for 5 min), coverslips were blocked with 4% bovine serum albumin (BSA) in PBS for 20 min at room temperature. After three washes with PBS, coverslips were incubated with the primary antibody diluted in PBS for 1 h at RT in a wet chamber followed by washes with PBS supplemented with 0.05% Tween 20 (PBS-T), for three times for 10 min. Subsequently, coverslips were incubated with corresponding secondary antibody for 1 h at RT in a wet chamber. After three washes in PBS-T, nuclei were stained with 0.2 µg/ml DAPI in PBS for 10 min and washed again in PBS (three times 5 min) at RT. To remove salts, coverslips were rinsed with water and mounted in non-hardening mounting medium (90% glycerol with 5% n-propylgalate). As a negative control, cells were incubated with secondary antibody only.

Image acquisition and reconstruction

SIM was performed on the Delta Vision OMX (Applied Precision) imaging system equipped with 3D structured illumination (3D-SIM) and a 60× oil immersion objective (NA 1.42, PlanApo N) and with a 4× pco.edge sCMOS

Journal of Cell Science (2017) 130, 2066-2077 doi:10.1242/jcs.198424

camera. Images were illuminated by lasers of wavelength of 405 nm, 488 nm and 568 nm, and collected using filter sets for blue (395.5/435.5), green (477.0/528.0) and red (571.0/609.0) fluorescence. For *z*-stacks, 0.125 µm optical sections were acquired. For the image reconstruction and registration, the SoftWorx (Applied Precision) software implemented with the 3D SI Reconstruction function was used; Wiener filter values were set to 0.001. Samples were mounted with 2,2′-thiodiethanol-n-propyl gallate antifade mounting (Life Technologies, Carlsbad, CA). Prior to image analysis, the quality of reconstructed images was checked using the SIMCheck toolbox (Ball et al., 2015).

The DeltaVision OMX system 3D-SIM provides a lateral resolution of ∼110 nm±5 nm in the 405 nm channel, 120 nm±5 nm in 488 nm channel, and 135±5 nm in 568 nm channel. Prior to imaging, the lateral resolution, as well as quality of registration, had been checked by using TetraSpeck microspheres (cat. no. T2729, Thermo Fisher Scientific, Waltham, MA) of defined width of 100 nm. We acquired a series of images of beads and analyzed the bead width. The results showed that for the excitation wavelength of 488 nm, the full width at half maximum (FWHM) of beads was 119.6±8.9 nm (mean±s.d.; n=10); for the excitation wavelength of 568 nm, the FWHM was 147.2±5.6 nm (mean±s.d.; n=10).

Automatic segmentation

The automatic segmentation routines were written in MATLAB (Release 2015a, The MathWorks, Inc., Natick, MA). 3D images acquired by SIM (see above) were used both for an identification of NPCs and an evaluation of fluorescence intensities of proteins of interest in the vicinity of the NPCs.

Prior to segmentation, the images were adjusted using Fiji software (Schindelin et al., 2012) to remove signal from neighboring nuclei as well as from the cytoplasm in 405 and 555 nm channels. This was performed to select the nucleus of interest and to standardize a normalization step. Nuclei as seen in the 405 and 555 nm channels (stained for DAPI and Nup62) had a border drawn on manually (Polygon selection tool), and the area outside the nuclei was cleared (Clear outside tool). Then, the MATLAB software tool was used for further analysis.

We have developed algorithms in MATLAB to identify NPCs in transversal *z*-sections of the cell nucleus (*z*-stack). An overview of the full segmentation process is presented in Fig. S1. The final result of the segmentation process is presented in Fig. 1B,C and Fig. S1I. These custom algorithms are available from the corresponding author upon request.

As the first step, the NPCs were identified based on their relative fluorescence intensity level (Fig. S1A,B). The mammalian NPC has a diameter of ∼120 nm and the length of the basket of the NPCs is ∼100 nm. In the OMX SIM image, the pixel size is 40 nm×40 nm, thus, the NPC basket is covered by a matrix of 3×3 pixels (black squares in Fig. 1E,G). Each *z*-section was thresholded at 20% of the maximum measured intensity level producing a binary image (Fig. S1B,C). This threshold intensity level was determined according to a test data containing three data series of at least 10 nuclei each that were not used in the final results. The watershed algorithm was applied to the binary image to separate individual NPCs and then the centroid of each object was identified (Fig. S1B,C).

In each *z*-section, objects resembling NPCs could be found both inside and outside the NE (Fig. S1A,B, arrowheads). Expecting a roughly elliptical shape of the nucleus in a *z*-section, a convex hull was used as a first approximation to define the initial shape of the NE (Fig. S1D). At this stage, some objects were identified that did not belong to the elliptical chain of the NPCs (Fig. S1D, arrowheads). To exclude those, we iteratively shifted the convex hull inside toward the real NE by applying geometrical constraints (distances and angles between adjacent NPCs) on the evolving curve (Fig. S1E). Specifically, we defined the minimum distance between the objects as 90 pixels (adjustable parameter) and the minimum angle between two neighboring pairs of NPCs as 161°. Finally, the curve was smoothed by using bicubic interpolation to mimic the NE (Fig. S1F). The objects located too far inside the nucleus (more than 2 pixels distant from the tangent to the NE, adjusted according to the test data) were removed as well, these were assumed not to correspond to the NPCs belonging to the NE and would be difficult to analyze due to the necessity to construct the normal vector to the NE (Fig. S1F, arrowhead). The mNPCs were identified so that the minimal distance between two identifiable NPCs was set to 5 pixels, to prevent overlaps between neighboring NPCs (adjustable parameter; Fig. S1H, red stars and Fig. 1B–D, red stars). Finally, the putative curve delineating the NE was approved by a human operator and disputable *z*-sections were removed.

To determine the NPC-free areas at the NE (referred to as mNEs), we looked for regional intensity minima (function imregionalmin in MATLAB, taking into account intensities of neighboring pixels) on the previously determined NE curve between all detected NPCs, and found that several minima could be identified in between a pair of two neighboring NPCs. According to the constraints on the minimum distances between mNPCs and mNEs, and mNEs themselves (all set to 5 pixels, adjustable parameters), we identified the positions of the resulting mNEs (see Fig. 1D, green stars; Fig. S1H,I, green stars).

Only the NPCs with relatively high fluorescence intensity (at least 50% of the maximum measured intensity level in each *z*-section) were used for further analysis, in order to only take into account NPCs with their centers located at the respective *z*-sections and not in neighboring *z*-sections. Finally, the software correction for errors was applied, including the deletion of continuous regions of mNPCs and mNE in which NPCs were located too far inside the nucleus (a cluster of at least two NPCs that were located more than 2 pixels inside and were less than 30 pixels in length along the NE). These sections represented concave parts of the NE and were not suitable for the analysis. Owing to the large amount of data (usually at least 2000 mNPCs or mNEs per experiment) it was impossible to manually correct the identified mNPCs and mNEs; however, images of whole-cell nuclei with segmented objects were manually checked and the nuclei and/or *z*-sections with an incorrectly defined NE were excluded from the analysis.

Collection of fluorescence intensity data

Following the determination of mNPCs and mNEs, we collected fluorescence intensities of the labeled proteins of interest using the positions of the segmented NPCs. The intensity data were collected along the NE tangent towards the inside and outside of the nucleus. To analyze the chromatin organization around the NPC, and to compare the values with the NPC-free areas at the NE, we analyzed the areas of mNPCs and mNE for 7×10 pixels (it corresponds to 280 nm along the NP and 400 nm into the nuclear interior; Fig. 1D). Owing to the minimum distance of 5 pixels that had been set between any two objects, the central 5 pixels (along the x axis, in graphs designated as pixel nos 0, 1 and 2) could never overlap with the corresponding central 5 pixels of the neighboring areas; however, the second and third pixel of the area could overlap with neighboring area. Overlaps of 3 pixels occurred in at most 9% of cases, of 2 pixels in 9% of cases and 1 pixel in 2% of cases.

Normalization and statistical analysis

We normalized fluorescence intensities among individual cell nuclei and *z*-slices. We computed the median of non-zero fluorescence intensities in the automatically segmented nuclear area for the 488 nm channel, which we used to detect a protein of interest. To normalize fluorescence intensities in each *z*-section (correction for bleaching), we divided the intensities by the median.

Before the analysis itself, we checked our data with respect to the heterogeneity within individual NPCs, individual sections and experiments. We found that the heterogeneity was similar across the mNE and mNPC areas as well as individual sections. We checked the distribution of the data, their mean, minimum and maximum values after data collection and after the normalization step. As the normalized fluorescence intensity did not differ between samples or sample sections, we pooled all the measured data. The median fluorescence intensity for pooled mNPCs as well as data for mNEs were plotted in a heat map such that the color of each individual pixel corresponded to the median fluorescence intensity of all measured data within one sample (Fig. 1E,F). Then, the median values of fluorescence intensity of the mNEs were subtracted from the median values of the fluorescence intensity of the mNPCs and result plotted in a heat-map (Fig. 1G). For purposes of statistical analysis, the fluorescence intensities were square root-transformed to bring their distributions, which were a slightly skewed right, closer to normal, and bootstrap was used to test the hypothesis of equal distributions of fluorescence intensities around mNPCs

and mNEs. The bootstrap procedure compared the observed difference in the means of intensities around mNPCs and mNEs to 9999 bootstrap-resampled differences (Efron and Tibshirani, 1993). This bootstrap procedure was repeated for each pixel around mNPCs and mNEs, yielding a *P*-value for each pixel. To adjust the *P*-values for the number of pixels, we followed the false discovery rate (FDR) approach according to Benjamini and Yekutieli (2001), and significantly different areas with a FDR-corrected *P*-value of less than 5% were bordered with a yellow line (Fig. 1G). For comparison purposes, we also used a two-sample *t*-test with unpooled variance estimates to test the hypothesis of equal means of fluorescence intensities around mNPCs and mNEs. This approach resulted in almost identical results to the computer-intensive bootstrap testing, but we continued to use the bootstrap test because of its greater robustness and its biologically appealing ability to detect general differences in the distributions of fluorescence intensities.

In total, each individual data set corresponded to normalized fluorescent intensity of individual pixels of mNPCs or mNEs that were usually within 3–10 *z*-sections per nucleus and at least 10 nuclei per sample. Thus, in total ~2000–8000 mNPCs or mNEs were analyzed per individual experiment. Five biological replicates were performed to study the distribution of active and inactive modifications at NPCs (Figs 3 and 4) with 50 nuclei in total collected for each variant. For the AMD study, we also discerned the localization of histone demethylases; 40 nuclei were collected in four independent biological replicates for each variant.

High-pressure freezing and freeze substitution of HeLa cells for TEM

The protocol according to Fišerová et al. (2016) was adopted.

Chemical fixation of HeLa cells for TEM

Cells were fixed for 40 min at room temperature in 3% paraformaldehyde and 0.1% glutaraldehyde in Sörensen buffer (SB; 0.1 M Na/K phosphate buffer, pH 7.3). Upon washing in SB (including 20 min of incubation in 20 mM glycine in SB), the cells were centrifuged (500 ***g*** for 10 min) into 1% low-melting agarose type VII (Sigma) in SB. The agarose-embedded cell samples were quickly dehydrated in a pre-cooled ethanol series (30%, 50%, 70%, 96% and 100%) and embedded in LR White resin (Polysciences Inc., Warrington, PA) with polymerization under UV light for 48 h at 4°C.

Immunogold labeling and TEM

80 nm sections were immunolabeled in a standard way (Hozak et al., 1994). Sections were examined and images acquired either with Philips Morgagni electron microscope equipped with a CCD Mega View III camera in a non-filtering mode.

SDS-PAGE and western blotting

The SDS-PAGE and western blotting were performed as described in Marasek et al. (2015).

Acknowledgements

We thank Iva Jelinkova for her help with immunofluorescence and HeLa cell culture, Karel Fiser for valuable discussions over the manuscript, and Martin W. Goldberg for comments and help with manuscript editing. We thank the Core Facility Microscopy Centre for help with SIM imaging.

Competing interests

The authors declare no competing or financial interests.

Author contributions

Conceptualization: J.F., P.H.; Methodology: J.F.; Software: M.E., T.S.; Validation: J.F., M.E., T.S.; Formal analysis: J.F., T.S., M.M., J.U.; Investigation: J.F., M.M.; Writing - original draft: J.F.; Writing - review & editing: J.F., M.E., T.S., M.M., P.H.; Visualization: M.M.; Supervision: J.F.; Funding acquisition: J.F.

Funding

This work was supported by the Grant Agency of the Czech Republic (Grantová Agentura České Republiky) [15-08835Y] through the institutional support of long-term conceptual support of development of the scientific organization (RVO: 68378050). We acknowledge the Microscopy Centre – Light/Electron CF, IMG AS CR supported by the Ministry of Education, Youth and Sports (Ministerstvo Školství, Mládeže a Tělovýchovy; MEYS) (LM2015062 Czech-BioImaging).

Data availability

Custom algorithms for detection of NPCs are available from the corresponding author upon request.

Supplementary information

Supplementary information available online at
http://jcs.biologists.org/lookup/doi/10.1242/jcs.198424.supplemental

References

Ball, G., Demmerle, J., Kaufmann, R., Davis, I., Dobbie, I. M. and Schermelleh, L. (2015). SIMcheck: a toolbox for successful super-resolution structured illumination microscopy. *Sci. Rep.* **5**, 15915.

Bannister, A. J. and Kouzarides, T. (2011). Regulation of chromatin by histone modifications. *Cell Res.* **21**, 381-395.

Belmont, A. S., Zhai, Y. and Thilenius, A. (1993). Lamin B distribution and association with peripheral chromatin revealed by optical sectioning and electron microscopy tomography. *J. Cell Biol.* **123**, 1671-1685.

Benjamini, Y. and Yekutieli, D. (2001). The control of the false discovery rate in multiple testing under dependency. *Ann. Stat.* **29**, 1165-1188.

Bickmore, W. A. and van Steensel, B. (2013). Genome architecture: domain organization of interphase chromosomes. *Cell* **152**, 1270-1284.

Blobel, G. (1985). Gene gating: a hypothesis. *Proc. Natl. Acad. Sci. USA* **82**, 8527-8529.

Brown, C. R., Kennedy, C. J., Delmar, V. A., Forbes, D. J. and Silver, P. A. (2008). Global histone acetylation induces functional genomic reorganization at mammalian nuclear pore complexes. *Genes Dev.* **22**, 627-639.

Capelson, M. and Hetzer, M. W. (2009). The role of nuclear pores in gene regulation, development and disease. *EMBO Rep.* **10**, 697-705.

Cavalli, G. and Misteli, T. (2013). Functional implications of genome topology. *Nat. Struct. Mol. Biol.* **20**, 290-299.

Eberhart, A., Feodorova, Y., Song, C., Wanner, G., Kiseleva, E., Furukawa, T., Kimura, H., Schotta, G., Leonhardt, H., Joffe, B. et al. (2013). Epigenetics of eu- and heterochromatin in inverted and conventional nuclei from mouse retina. *Chromosome Res.* **21**, 535-554.

Efron, B. and Tibshirani, R. (1993). *An Introduction to the Bootstrap*. Chapman & Hall/CRC.

Egecioglu, D. and Brickner, J. H. (2011). Gene positioning and expression. *Curr. Opin. Cell Biol.* **23**, 338-345.

Egelhofer, T. A., Minoda, A., Klugman, S., Lee, K., Kolasinska-Zwierz, P., Alekseyenko, A. A., Cheung, M.-S., Day, D. S., Gadel, S., Gorchakov, A. A. et al. (2011). An assessment of histone-modification antibody quality. *Nat. Struct. Mol. Biol.* **18**, 91-93.

Fišerová, J., Richardson, C. and Goldberg, M. W. (2016). Immunoelectron microscopy of cryofixed freeze-substituted yeast Saccharomyces cerevisiae. *Methods Mol. Biol.* **1474**, 243-258.

Frosst, P., Guan, T., Subauste, C., Hahn, K. and Gerace, L. (2002). Tpr is localized within the nuclear basket of the pore complex and has a role in nuclear protein export. *J. Cell Biol.* **156**, 617-630.

Galy, V., Olivo-Marin, J.-C., Scherthan, H., Doye, V., Rascalou, N. and Nehrbass, U. (2000). Nuclear pore complexes in the organization of silent telomeric chromatin. *Nature* **403**, 108-112.

Gruenbaum, Y. and Foisner, R. (2015). Lamins: nuclear intermediate filament proteins with fundamental functions in nuclear mechanics and genome regulation. *Annu. Rev. Biochem.* **84**, 131-164.

Guelen, L., Pagie, L., Brasset, E., Meuleman, W., Faza, M. B., Talhout, W., Eussen, B. H., de Klein, A., Wessels, L., de Laat, W. et al. (2008). Domain organization of human chromosomes revealed by mapping of nuclear lamina interactions. *Nature* **453**, 948-951.

Harr, J. C., Gonzalez-Sandoval, A. and Gasser, S. M. (2016). Histones and histone modifications in perinuclear chromatin anchoring: from yeast to man. *EMBO Rep.* **17**, 139-155.

Hozak, P., Jackson, D. A. and Cook, P. R. (1994). Replication factories and nuclear bodies: the ultrastructural characterization of replication sites during the cell cycle. *J. Cell Sci.* **107**, 2191-2202.

Iborra, F. J., Jackson, D. A. and Cook, P. R. (2000). The path of RNA through nuclear pores: apparent entry from the sides into specialized pores. *J. Cell Sci.* **113**, 291-302.

Kalverda, B., Pickersgill, H., Shloma, V. V. and Fornerod, M. (2010). Nucleoporins directly stimulate expression of developmental and cell-cycle genes inside the nucleoplasm. *Cell* **140**, 360-371.

Kehat, I., Accornero, F., Aronow, B. J. and Molkentin, J. D. (2011). Modulation of chromatin position and gene expression by HDAC4 interaction with nucleoporins. *J. Cell Biol.* **193**, 21-29.

Kind, J., Pagie, L., Ortabozkoyun, H., Boyle, S., de Vries, S. S., Janssen, H., Amendola, M., Nolen, L. D., Bickmore, W. A. and van Steensel, B. (2013). Single-cell dynamics of genome-nuclear lamina interactions. *Cell* **153**, 178-192.
Kooistra, S. M. and Helin, K. (2012). Molecular mechanisms and potential functions of histone demethylases. *Nat. Rev. Mol. Cell Biol.* **13**, 297-311.
Krull, S., Dorries, J., Boysen, B., Reidenbach, S., Magnius, L., Norder, H., Thyberg, J. and Cordes, V. C. (2010). Protein Tpr is required for establishing nuclear pore-associated zones of heterochromatin exclusion. *EMBO J.* **29**, 1659-1673.
Liang, Y., Franks, T. M., Marchetto, M. C., Gage, F. H. and Hetzer, M. W. (2013). Dynamic association of NUP98 with the human genome. *PLoS Genet.* **9**, e1003308.
Light, W. H., Brickner, D. G., Brand, V. R. and Brickner, J. H. (2010). Interaction of a DNA zip code with the nuclear pore complex promotes H2A.Z incorporation and INO1 transcriptional memory. *Mol. Cell* **40**, 112-125.
Marasek, P., Dzijak, R., Studenyak, I., Fiserova, J., Ulicna, L., Novak, P. and Hozak, P. (2015). Paxillin-dependent regulation of IGF2 and H19 gene cluster expression. *J. Cell Sci.* **128**, 3106-3116.
Markaki, Y., Smeets, D., Fiedler, S., Schmid, V. J., Schermelleh, L., Cremer, T. and Cremer, M. (2012). The potential of 3D-FISH and super-resolution structured illumination microscopy for studies of 3D nuclear architecture: 3D structured illumination microscopy of defined chromosomal structures visualized by 3D (immuno)-FISH opens new perspectives for studies of nuclear architecture. *BioEssays* **34**, 412-426.
Meldi, L. and Brickner, J. H. (2011). Compartmentalization of the nucleus. *Trends Cell Biol.* **21**, 701-708.
Pal-Bhadra, M., Leibovitch, B. A., Gandhi, S. G., Chikka, M. R., Bhadra, U., Birchler, J. A. and Elgin, S. C. (2004). Heterochromatic silencing and HP1 localization in Drosophila are dependent on the RNAi machinery. *Science* **303**, 669-672.
Pascual-Garcia, P. and Capelson, M. (2014). Nuclear pores as versatile platforms for gene regulation. *Curr. Opin. Genet. Dev.* **25**, 110-117.
Pickersgill, H., Kalverda, B., de Wit, E., Talhout, W., Fornerod, M. and van Steensel, B. (2006). Characterization of the Drosophila melanogaster genome at the nuclear lamina. *Nat. Genet.* **38**, 1005-1014.
Raices, M. and D'Angelo, M. A. (2012). Nuclear pore complex composition: a new regulator of tissue-specific and developmental functions. *Nat. Rev. Mol. Cell Biol.* **13**, 687-699.
Reik, W. (2007). Stability and flexibility of epigenetic gene regulation in mammalian development. *Nature* **447**, 425-432.
Ruben, G. J., Kirkland, J. G., MacDonough, T., Chen, M., Dubey, R. N., Gartenberg, M. R. and Kamakaka, R. T. (2011). Nucleoporin mediated nuclear positioning and silencing of HMR. *PLoS ONE* **6**, e21923.
Sadaie, M., Salama, R., Carroll, T., Tomimatsu, K., Chandra, T., Young, A. R. J., Narita, M., Perez-Mancera, P. A., Bennett, D. C., Chong, H. et al. (2013). Redistribution of the Lamin B1 genomic binding profile affects rearrangement of heterochromatic domains and SAHF formation during senescence. *Genes Dev.* **27**, 1800-1808.
Schermelleh, L., Carlton, P. M., Haase, S., Shao, L., Winoto, L., Kner, P., Burke, B., Cardoso, M. C., Agard, D. A., Gustafsson, M. G. L. et al. (2008). Subdiffraction multicolor imaging of the nuclear periphery with 3D structured illumination microscopy. *Science* **320**, 1332-1336.
Schindelin, J., Arganda-Carreras, I., Frise, E., Kaynig, V., Longair, M., Pietzsch, T., Preibisch, S., Rueden, C., Saalfeld, S., Schmid, B. et al. (2012). Fiji: an open-source platform for biological-image analysis. *Nat. Methods* **9**, 676-682.
Schotta, G., Lachner, M., Sarma, K., Ebert, A., Sengupta, R., Reuter, G., Reinberg, D. and Jenuwein, T. (2004). A silencing pathway to induce H3-K9 and H4-K20 trimethylation at constitutive heterochromatin. *Genes Dev.* **18**, 1251-1262.
Shah, P. P., Donahue, G., Otte, G. L., Capell, B. C., Nelson, D. M., Cao, K., Aggarwala, V., Cruickshanks, H. A., Rai, T. S., McBryan, T. et al. (2013). Lamin B1 depletion in senescent cells triggers large-scale changes in gene expression and the chromatin landscape. *Genes Dev.* **27**, 1787-1799.
Shimi, T., Pfleghaar, K., Kojima, S., Pack, C.-G., Solovei, I., Goldman, A. E., Adam, S. A., Shumaker, D. K., Kinjo, M., Cremer, T. et al. (2008). The A- and B-type nuclear lamin networks: microdomains involved in chromatin organization and transcription. *Genes Dev.* **22**, 3409-3421.
Shimi, T., Kittisopikul, M., Tran, J., Goldman, A. E., Adam, S. A., Zheng, Y., Jaqaman, K. and Goldman, R. D. (2015). Structural organization of nuclear lamins A, C, B1, and B2 revealed by superresolution microscopy. *Mol. Biol. Cell* **26**, 4075-4086.
Strambio-De-Castillia, C., Niepel, M. and Rout, M. P. (2010). The nuclear pore complex: bridging nuclear transport and gene regulation. *Nat. Rev. Mol. Cell Biol.* **11**, 490-501.
Szymborska, A., de Marco, A., Daigle, N., Cordes, V. C., Briggs, J. A. G. and Ellenberg, J. (2013). Nuclear pore scaffold structure analyzed by super-resolution microscopy and particle averaging. *Science* **341**, 655-658.
Taddei, A., Van Houwe, G., Hediger, F., Kalck, V., Cubizolles, F., Schober, H. and Gasser, S. M. (2006). Nuclear pore association confers optimal expression levels for an inducible yeast gene. *Nature* **441**, 774-778.
Talamas, J. A. and Capelson, M. (2015). Nuclear envelope and genome interactions in cell fate. *Front. Genet.* **6**, 95.
Ueda, J., Maehara, K., Mashiko, D., Ichinose, T., Yao, T., Hori, M., Sato, Y., Kimura, H., Ohkawa, Y. and Yamagata, K. (2014). Heterochromatin dynamics during the differentiation process revealed by the DNA methylation reporter mouse, MethylRO. *Stem Cell Rep.* **2**, 910-924.
Van Bortle, K. and Corces, V. G. (2012). Nuclear organization and genome function. *Annu. Rev. Cell Dev. Biol.* **28**, 163-187.
Van de Vosse, D. W., Wan, Y., Lapetina, D. L., Chen, W.-M., Chiang, J.-H., Aitchison, J. D. and Wozniak, R. W. (2013). A role for the nucleoporin Nup170p in chromatin structure and gene silencing. *Cell* **152**, 969-983.
van Rij, R. P., Saleh, M.-C., Berry, B., Foo, C., Houk, A., Antoniewski, C. and Andino, R. (2006). The RNA silencing endonuclease Argonaute 2 mediates specific antiviral immunity in Drosophila melanogaster. *Genes Dev.* **20**, 2985-2995.
Vandamme, J., Sidoli, S., Mariani, L., Friis, C., Christensen, J., Helin, K., Jensen, O. N. and Salcini, A. E. (2015). H3K23me2 is a new heterochromatic mark in Caenorhabditis elegans. *Nucleic Acids Res.* **43**, 9694-9710.
Visser, A. E., Jaunin, F., Fakan, S. and Aten, J. A. (2000). High resolution analysis of interphase chromosome domains. *J. Cell Sci.* **113**, 2585-2593.
Volpe, T. A., Kidner, C., Hall, I. M., Teng, G., Grewal, S. I. and Martienssen, R. A. (2002). Regulation of heterochromatic silencing and histone H3 lysine-9 methylation by RNAi. *Science* **297**, 1833-1837.
Wang, X.-H., Aliyari, R., Li, W.-X., Li, H.-W., Kim, K., Carthew, R., Atkinson, P. and Ding, S.-W. (2006). RNA interference directs innate immunity against viruses in adult Drosophila. *Science* **312**, 452-454.
Waters, J. C. (2009). Accuracy and precision in quantitative fluorescence microscopy. *J. Cell Biol.* **185**, 1135-1148.
Wu, R., Terry, A. V., Singh, P. B. and Gilbert, D. M. (2005). Differential subnuclear localization and replication timing of histone H3 lysine 9 methylation states. *Mol. Biol. Cell* **16**, 2872-2881.
Yokochi, T., Poduch, K., Ryba, T., Lu, J., Hiratani, I., Tachibana, M., Shinkai, Y. and Gilbert, D. M. (2009). G9a selectively represses a class of late-replicating genes at the nuclear periphery. *Proc. Natl. Acad. Sci. USA* **106**, 19363-19368.